Catalytic Dehydration of Ethanol over WO$_x$ Nanoparticles Supported on MFI (Mobile Five) Zeolite Nanosheets

Haneul Kim [2,†], Muhammad Numan [1,†] and Changbum Jo [1,2,*]

1   Department of Chemistry and Chemical Engineering, Inha University, Incheon 22212, Korea
2   Department of Chemistry, Inha University, Incheon 22212, Korea
*   Correspondence: jochangbum@inha.ac.kr
†   These authors contributed equally.

Abstract: Ethylene can be synthesized in a renewable manner by dehydrating bioethanol over supported metal oxide nanoparticle catalysts. Here, a series of nanoparticulate tungsten oxides supported on MFI (Mobil five) zeolite nanosheets was prepared at different W loadings (1 to 6 mol %) using the incipient wetness method and investigated with respect to the ability to catalyze the dehydration of ethanol. The resulting samples were characterized by X-ray diffraction, electron microscopy, N$_2$ isotherms, X-ray absorption fine structures, and by the temperature-programmed desorption of NH$_3$. The results obtained showed that WO$_x$ nanoparticles were homogeneously distributed over the entire void space of nanosheet samples up to a loading of 2 mol %, after which large WO$_x$ nanoparticles with needle-like morphology were formed on the surface of the zeolite nanosheet beyond 2mol%. The number of acid sites increased with WO$_x$ loading and, as a result, EtOH conversion progressively increased with WO$_x$ loading up to 6 mol %. At reaction temperatures of >390 °C, homogeneously distributed WO$_x$ nanoparticles showed slightly higher ethylene selectivity than nano-needle structured WO$_x$. However, nano-needle structured WO$_x$ exhibited greater catalytic stability. In terms of ethylene yield over 8 h, needle-like WO$_x$ nanoparticles were found to be more suitable for the acid-catalyzed dehydration of ethanol than small-sized WO$_x$ nanoparticles.

Keywords: ethanol dehydration; supported tungsten oxide; MFI zeolite; zeolite nanosheet

1. Introduction

In the petrochemical industry, demand for light olefins (ethylene and propylene) is increasing daily and is currently at record levels [1]. Presently, global ethylene production is around 150 million tons per year and is expected to increase [1]. Ethylene is widely used to produce ethylene glycol as antifreeze and many organic materials, such as ethylene dichloride, acetaldehyde, acetic acid, ethylene glycol, chloroethanol, and vinyl acetate [2–4]. Nowadays, over 90% of ethylene is produced using the naphtha steam cracking process at temperatures of 750 to 900 °C [2–5], which requires huge amounts of energy and generates massive amounts of carbon dioxide [6]. To overcome these problems, large investments were made in the development of new catalytic pathways for sustainable ethylene production and these developments resulted in processes such as the catalytic dehydrogenation of light alkanes and the dehydration of bioethanol. Of these raw materials, bioethanol is considered a clean, renewable source because it can be easily produced by microbial fermentation [2,7]. In addition, catalytic dehydration is a preferred pathway because it preserves biomass carbon content and generates water as the only byproduct [8]. However, as mentioned above, catalytic dehydration requires high temperatures (300–500 °C), thus, reducing the temperature required for catalytic dehydration has become a major developmental objective [3,9].

Several studies have investigated the dehydration of ethanol over heterogeneous acid catalysts, such as H-forms of zeolites, γ-Al$_2$O$_3$, and metal-supported catalysts [10–14]. Microporous acid catalysts (e.g., zeolite and silicoaluminophosphate) have strong acid sites in their micropores, thus, they can effectively catalyze dehydration with high activity and selectivity at relatively mild temperatures (200–350 °C) [15]. The type of acid site, such as a Lewis acid or a Brønsted acid, is a key factor in the EtOH dehydration reaction [16]. Busca characterized the acid sites of several commercial zeolites using Fourier-transform infrared spectroscopy of the surface OH groups and adsorbed CO and pyridine and investigated zeolite catalytic activity with relation to acid sites [16]. Takahara et al. examined ethanol dehydration over several zeolites and concluded that ethylene formation was favored by strong acid sites and diethyl ether production by weak acid sites [17]. In addition, these authors showed ethylene could also be produced from diethyl ether. However, the zeolite catalysts used were rapidly deactivated due to coke formation in micropores that restricted ethanol access to acid sites in micropores [17]. Recently, mesoporous materials, such as MCM-41, SBA-15, and KIT-6, have attracted much attention as alternatives to zeolite catalysts [18–20]. Haishi et al. reported Al-incorporated MCM-41 yielded almost 100% ethylene at 430 °C [21]. However, large amounts of Al-MCM-41 catalysts and high reaction temperatures are required to achieve complete EtOH conversion because they have much lower acidities than zeolite catalysts. These low acidities of Al-MCM-41 catalysts are attributed to the fact that mesoporous silica is built with an amorphous framework. Instead of using aluminum, Subramaniam directly synthesized ordered mesoporous KIT-6 containing several transition metals (e.g., W, Zr, and Nb) [18,20,22,23]. The incorporation of transition metals created acid sites on the mesopore walls. In particular, the simultaneous incorporation of W and Zr into KIT-6 generated strong Brønsted acid sites on mesopore walls, which were as acidic as those found in zeolites [18]. As a result, the W/Zr KIT-6 catalysts achieved ethylene yields approaching those reported for HZSM-5 (H$^+$ form of Zeolite Socony Mobil-5) under similar reaction conditions [18]. Recently, Osman et al. reported that supporting copper in mesoporous alumina enhances surface hydrophobicity, which increases the reaction rate of dehydration [24].

Recently, Ryoo et al., reported the synthesis of MFI zeolite nanosheets (ZNs) using a di-quaternary ammonium surfactant as the zeolite structure-directing agent (SDA) [25–28]. ZNs have an MFI (Mobil Five, ZSM (Zeolite Socony Mobil)-5) framework topology and a nanosheet thickness of 2.5 nm, which are assembled to form a mesostructure. MFI ZN structures may be multilayer or unilayer sheets, or may have a nanosponge morphology depending on synthetic conditions [27,29]. MFI ZNs have much greater thermal, hydrothermal, and mechanical stabilities than mesoporous silicas because of their crystalline zeolitic frameworks [30]. Furthermore, various metals or metal oxides can be supported by MFI zeolite nanosheets in the form of highly dispersed nanoparticles [31] and these supported nanoparticles have high catalytic activities [32–35]. Due to the stability of the frameworks and the high levels of metal dispersion achieved, mesoporous MFI zeolites have attracted much attention as potential support materials for a wide range of catalytic reactions.

In this work, we loaded different amounts of tungsten oxides onto MFI ZN samples and characterized the supported WO$_x$ catalysts produced by X-ray diffraction (XRD), scanning transmission microscopy (STEM), N$_2$ adsorption-desorption isotherm analysis, X-ray absorption fine structure (XAFS) analysis, and by the temperature-programmed desorption (TPD) of NH$_3$. Furthermore, the catalytic activities and selectivity of the series of supported WO$_x$ catalysts produced were investigated in the context of EtOH dehydration. Notably, the morphologies of the supported WO$_x$ nanoparticles on the nanosheet MFI zeolite depended on their loadings and, consequently, altered their selectivities and stabilities.

2. Results and Discussions

2.1. Supporting Tungsten Oxide Nanoparticle on MFI Zeolite Nanosheets

Pure silica MFI zeolite nanosheets (ZN) were synthesized using a di-quaternary ammonium surfactant as the zeolite SDA, as previously described [25]. XRD patterns and SEM and TEM results showed that resultant samples were 2.5 nm-thick zeolite nanosheets with MFI structures (Figure S1). Due to their extremely low thicknesses, the zeolite nanosheets had a large external surface area ($642 \ m^2 \ g^{-1}$) and a large mesopore volume ($0.71 \ cm^3 \ g^{-1}$), which made them suitable for supporting nanoparticles. Different amounts of tungsten oxides (1, 2, 4, and 6 mol %) were impregnated into MFI ZNs. The resulting samples are denoted by m-WO_x ZN, where m indicates the amount of tungsten oxide loaded.

Figure 1 shows powder XRD patterns for 1-, 2-, 4-, and 6-WO_x ZN samples. The 1- and 2-WO_x ZN samples exhibited XRD peaks that were similar to those of the ZN support, but at reduced intensities. No XRD peaks corresponding to tungsten oxides were observed for 1- or 2-WO_x ZN samples, indicating high dispersion of tungsten oxide nanoparticles on supporting MFI zeolite nanosheets and the distribution of tungsten oxides on ZN as nanoclusters. However, at loadings of ≥4 mol%, several reflection peaks centered at 23.1, 23.7, 24.6, 27, 28.9, 33.4, 34.3, and 35.8 appeared in XRD patterns, which corresponded to the (002), (020), (200), (120), (112), (022), and (202) planes, respectively, of monoclinic ($P2_1/n$) WO_3 [36]. XRD results showed that, at tungsten oxide loadings of ≥4 mol%, larger particles were formed.
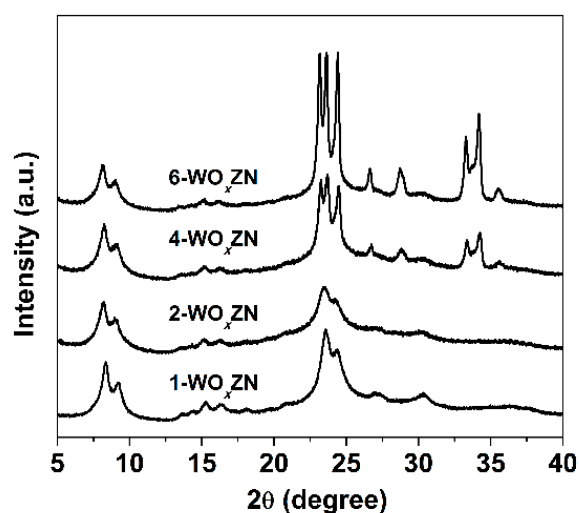
Figure 1. Powder X-ray diffraction patterns for 1-, 2-, 4-, and 6-WO_x zeolite nanosheet (ZN) samples.

Particle sizes and distributions of tungsten oxide nanoparticles on 1- and 4-WO_x ZN samples were investigated by Scanning transmission electron microscope (STEM) imaging. To enhance the contrast between WO_x nanoparticles and zeolite frameworks, a high-angle annular dark-field (HADDF) imaging detector was used [37]. In HAADF STEM images, atoms with higher atomic weights appear brighter, thus, the tungsten and zeolite frameworks appeared as bright and dark regions, respectively (see Figure 2b). Tungsten oxide nanoparticles were not observed by STEM on 1-WO_x ZN samples (Figure 2a), which indicated that tungsten oxides were distributed as very small nanoparticles over the ZN samples. In contrast, two types of tungsten oxide nanoparticles were observed on 4-WO_x ZN samples (Figure 2b), that is, needle-like nanoparticles, 10–30 nm in length (inset of Figure 2b) and 3–5 nm in width, and irregularly shaped, large nanoparticles, with diameters exceeding 50 nm. STEM results showed tungsten oxides were present as tiny nanoparticles on 1-WO_x ZN samples. However, as the loading amount of tungsten oxide increased, the tiny nanoparticles gradually disappeared. In the

case of 4- and 6-WO$_x$ ZN samples, a large portion of supported tungsten oxides had needle-shaped nanoparticles, which were larger than those of the 1-WO$_x$ ZN sample.
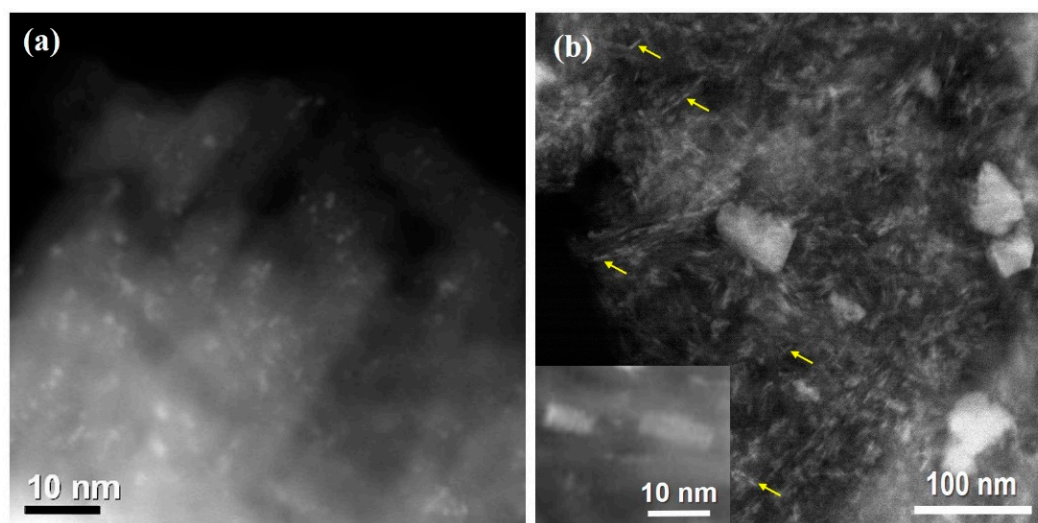
Figure 2. Scanning transmission electron microscope(STEM) images of (**a**) 1-WO$_x$ ZN and (**b**) 4-WO$_x$ ZN samples. Inset of Figure 2b is a magnified STEM image, showing needle-shaped WO$_X$ nanoparticles. Some needle-shape WO$_x$ nanoparticles are indicated as yellow arrows in (**b**).

Figure 3 shows N$_2$ adsorption–desorption isotherms for 1-, 2-, 4-, and 6-WO$_x$ ZN samples. All four samples exhibited type IV isotherms with adsorption steps at relative pressures of <0.1 and 0.4–0.8, which were similar to those observed for pristine ZN samples. Figure 3a shows that the 1-WO$_x$ ZN samples adsorbed a large amount of nitrogen (~ 120 m^2 g^{-1}) at a relative pressure (*P/P$_0$*) of ~0.01. This steep increase in N$_2$ adsorption at such a low *P/P$_0$* (i.e., relative pressure) level confirmed the presence of micropores in the samples. In addition, nitrogen was gradually adsorbed in the region 0.4 < *P/P$_0$* < 0.8, indicating mesopore availability in 1-WO$_x$ ZN samples. Due to its mesoporous structure, 1-WO$_x$ ZN had a large pore volume (~ 0.57 cm^3 g^{-1}) and specific surface area (~ 529 m^2 g^{-1}). When tungsten oxide loading was increased, pore volume and specific surface area decreased. The 6-WO$_x$ ZN samples had a specific surface area of 396 m^2 g^{-1} and a pore volume of ~0.49 cm^3 g^{-1}. Pore-structure characterization results derived from N$_2$ adsorption isotherms are summarized in Table 1.

Table 1. Pore characterization results for 1-WO$_x$ ZN, 2-WO$_x$ ZN, 4-WO$_x$ ZN, and 6-WO$_x$ ZN samples.

Catalyst	S_{BET} [a] (m^2 g^{-1})	S_{micro} [b] (m^2 g^{-1})	S_{ext} [c] (m^2 g^{-1})	V_{total} [d]
MFI	642	152	489	0.71
1-WO$_x$-MFI	529	152	377	0.57
2-WO$_x$-MFI	470	153	317	0.577
4-WO$_x$-MFI	387	149	239	0.51
6-WO$_x$-MFI	396	128	267	0.49

[a] S_{BET} is the BET(Brunauer, Emmett, and Teller) surface area, using relative pressure range of 0.05–0.3. [b] S_{micro} is the micropore surface area using the t-plot method. [c] S_{ext} is the external surface area calculated using the t-plot method. [d] V_{total} is total pore volume obtained at *P/P$_0$* = 0.95.
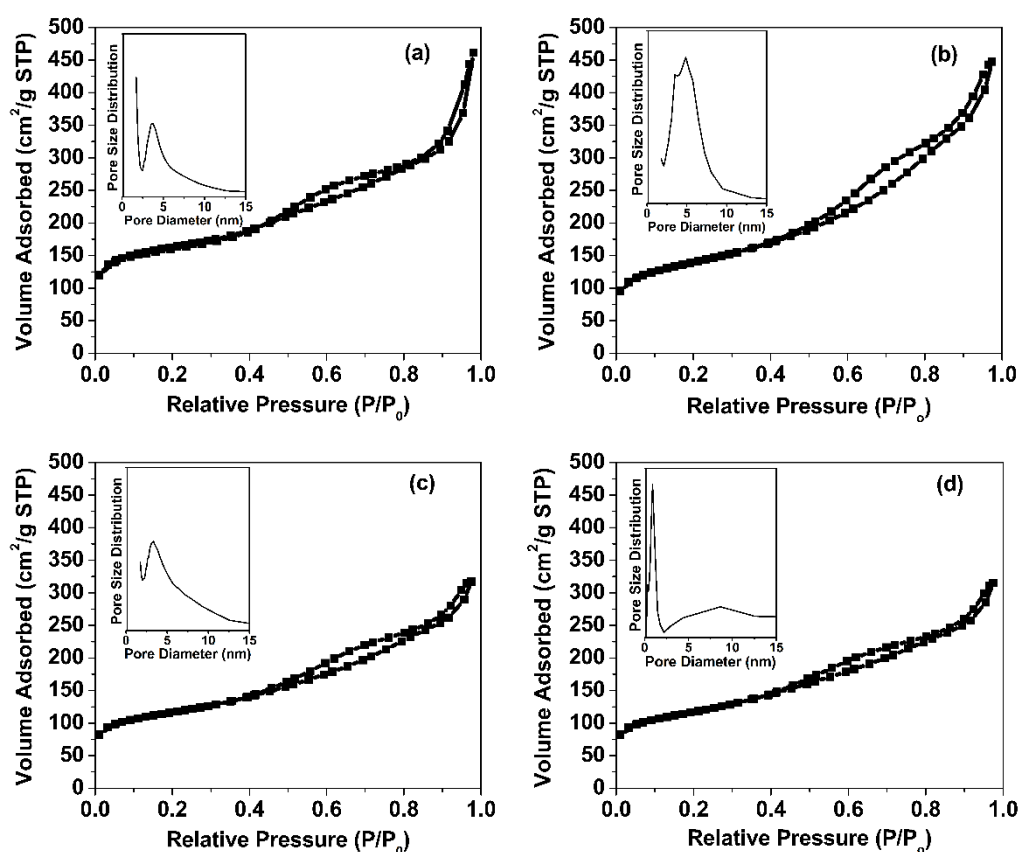
Figure 3. N_2 adsorption–desorption isotherms for (**a**) 1-WO_x ZN, (**b**) 2-WO_x ZN, (**c**) 4-WO_x ZN, and (**d**) 6-WO_x ZN samples. The BJH(Barrett, Joyner, and Halenda) pore size distribution derived from the adsorption branches of the isotherms is displayed in the inset.

Figure 4a shows W-L_3 X-ray absorption near edge structure (XANES) spectra for 1-, 2-, 4-, and 6-WO_x ZN samples. All four samples exhibited an absorption peak in the 10,210–10,220 eV range, centered at 10,213 eV. This result matched the typical W-L_3 XANES spectrum of W^{6+} in monoclinic WO_3 well (see Figure S2) [38] and indicated that the oxidation state of W in 1-, 2-, 4-, and 6-WO_x ZN samples was +6, irrespective of tungsten contents in the ZN supports. Figure S3 and Figure 4b show k^2-weighted W-L_3 edge and Fourier transform Extended X-ray absorption fine structure(EXAFS) spectra in R space of the 1-, 2-, 4-, and 6-WO_x ZN samples. As shown in Figure S3, the oscillation wavelengths of all supported samples were similar, indicating similar local tungsten oxide structures. We attempted to fit experimental EXAFS results with a W-O pair theoretically derived from crystallographic data of monoclinic WO_3 using the quick first shell mode. As shown by fitting results (Table 2), the W-O bond distance in the 1-, 2-, 4-, and 6-WO_x ZN samples was ~1.8 Å, which corresponded to the bond distance between W and the nearest oxygen atom in monoclinic WO_3. The coordination number (CN) of the 1-WO_x ZN sample was 3.6. The CNs increased with tungsten oxide loading, which confirmed that the particle size of tungsten oxide increased with loading. EXAFS results were in-line with XRD and STEM results.
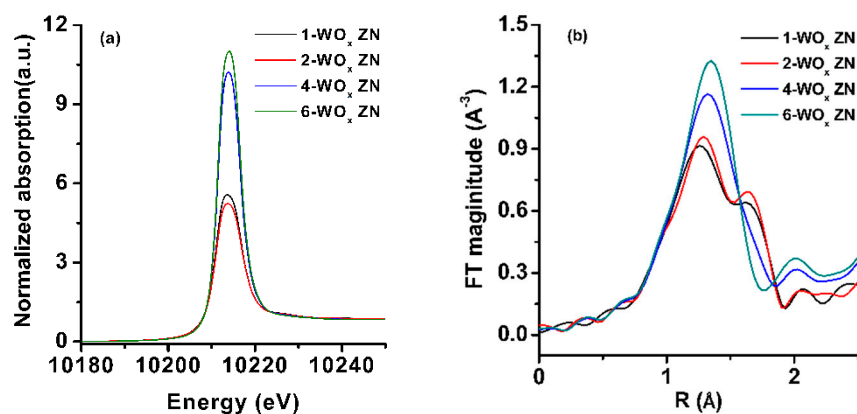
Figure 4. (**a**) The W-L$_3$ edge X-ray absorption near edge structure (XANES) and (**b**) Fourier transform(FT) (Extended X-ray absorption fine structure) EXAFS spectra in R (radial distance) space for 1-WO$_x$ ZN, 2-WO$_x$ ZN, 4-WO$_x$ ZN, and 6-WO$_x$ ZN samples.

Table 2. W L$_3$-edge EXAFS analysis of 1-WO$_x$ ZN, 2-WO$_x$ ZN, 4-WO$_x$ ZN, and 6-WO$_x$ ZN samples [a].

Sample	Shell	N [b]	R [c]	σ^{2} [d] $\times 10^{-3}$ Å^2	ΔE_0(eV) [e]	r-factor
1-WOx-ZN	W-O	3.6 ± 1.9	1.80 ± 0.05	17.5 ± 7.7	7.8 ± 7.0	0.019
2-WOx-ZN	W-O	4.1 ± 1.5	1.80 ± 0.1	16.5 ± 16.5	8.8 ± 5.0	0.022
4-WOx-ZN	W-O	4.8 ± 1.2	1.78 ± 0.02	10.5 ± 3.0	3.2 ± 3.2	0.011
6-WOx-ZN	W-O	5.1 ± 1.2	1.77 ± 0.02	6.2 ± 3.6	3.0 ± 4.6	0.026

[a] The analysis was carried out in the k range of 3–11 Å^{-1} with a k-weight of 2 and an R range of 1–2.2 Å. The uncertainties in the fitting result for the samples are provided. [b] N is the coordination number of W-O as obtained from EXAFS analysis. [c] R is the bond length as obtained from the EXAFS analysis. [d] σ^2 is the Debye-Waller factor. [e] ΔE_0 is the edge-energy shift.

The acidities of 1-, 2-, 4-, and 6-WO$_x$ ZN samples were assessed using the Temperature programmed desorption(TPD) of NH$_3$. As shown in Figure 5, all samples exhibited an asymmetric TPD peak in the range of 50 to 250 °C. This TPD peak was deconvoluted into two peaks centered at ~100 °C and ~150 °C, respectively. The lower temperature desorption peak (Type I) corresponded to weak acid sites, whereas the higher peak (Type II) corresponded to moderately acidic sites [39]. Numbers of weakly and moderately acidic sites were calculated from NH$_3$-TPD observations; these results are summarized in Table 3. As shown in the table, numbers of both types of acid sites increased with tungsten oxide loading, but type II sites increased more rapidly than type I sites. Consequently, Type II/Type I ratios increased with WO$_x$ loading.
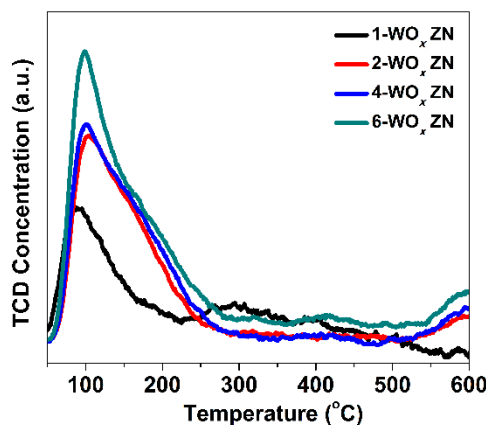
Figure 5. NH$_3$-Tempeature-programmed desorption of 1-WO$_x$ ZN, 2-WO$_x$ ZN, 4-WO$_x$ ZN, and 6-WO$_x$ ZN samples.

Table 3. NH$_3$-TPD results for 1-WO$_x$ ZN, 2-WO$_x$ ZN, 4-WO$_x$ ZN, and 6-WO$_x$ ZN samples.

Sample	Temperature of Desorption (°C)		Acid Amount (mmol g^{-1})		II/(I+II)	TOTAL
	I	II	I	II		
1-WOx-ZN	84.5	142	0.10	0.09	0.47	0.19
2-WOx-ZN	99	160	0.13	0.12	0.48	0.25
4-WOx-ZN	95	156	0.12	0.2	0.625	0.319
6-WOx-ZN	94.2	157	0.16	0.23	0.589	0.39

2.2. Ethanol Conversion Studies

To evaluate the catalytic reactivities of WO$_x$ ZN samples, ethanol dehydration was performed over the temperature range of 300–450 °C. During reactions, the major products with a selectivity of >1% were ethylene, ethane, acetaldehyde, and diethyl ether (DEE); minor products included methane, propylene, and others. Typical gas chromatograms obtained by online analysis are shown in Figure S4. Of those products, ethylene and acetaldehyde are formed by an intramolecular reaction, whereas DEE is formed by an intermolecular reaction [40]. Bhan et al. showed, using in situ pyridine titration experiments, that both reactions are catalyzed by acid sites [41]. Beta(β) C-H bond cleavage is the rate-limiting step in the synthesis of ethylene and, after this bond has been broken, ethylene is formed with the concomitant release of water [40]. On the other hand, acetaldehyde is formed after cleavage of an alpha(α) C-H bond and this is followed by the release of hydrogen [42]. In the case of DEE formation, it was proposed that the rate-limiting step is C-O bond cleavage in ethanol. Minor products are possibly generated by hydrocarbon cracking, ethylene dimerization, or metathesis reactions [40].

Figure 6 shows plots of EtOH conversion and ethylene selectivity as functions of reaction temperature at a fixed space velocity of 1.5 h^{-1} for the ZN-supported WO$_3$ samples that were synthesized. Plotted values represent average conversions and selectivity values over 2 h. As shown in Figure 6a, EtOH conversions increased with reaction temperature for all samples. At low reaction temperatures (i.e., low conversion levels), EtOH conversion increased in the order 1-WO$_x$ ZN < 2-WO$_x$ ZN < 4-WO$_x$ ZN < 6-WO$_x$ ZN. This tendency could be explained by numbers of acid sites, as indicated by the NH$_3$-TPD experiment. Bhan et al. also reported that ethanol conversion increased with the number of acid sites [41]. Figure 6b shows ethylene selectivity as a function of reaction temperature for the ZN-supported WO$_x$ samples. The ethylene selectivity exhibited the same tendency for all tested samples. Selectivity for ethylene was low at lower temperatures due to diethyl ether formation [15] and increased at higher temperatures at the expense of diethyl ether selectivity. The maximum selectivities for ethylene of 1-WO$_x$ ZN, 2-WO$_x$ ZN, 4-WO$_x$ ZN, and 6-WO$_x$ ZN were 92.9%, 92.6%, 91.7%, and 92.5%, respectively, at 450 °C. For comparison, commercial MFI zeolite with a Si/Al ratio of 23 (i.e., CBV 2314, zeolyst) was also tested. The results show that commercial MFI zeolite exhibited ~93.8% EtOH conversion and 44.3% ethylene selectivity at 300 °C at the weight hour space velocity (WHSV) of 1.5 h^{-1} (Table S1).
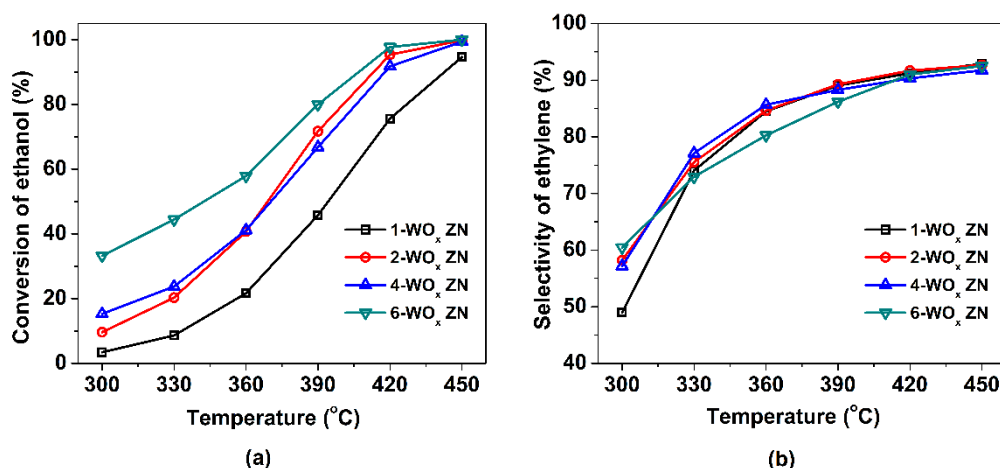
Figure 6. (**a**) Ethanol conversion and (**b**) ethylene selectivity as a function of reaction temperature over 1-WO$_x$ ZN, 2-WO$_x$ ZN, 4-WO$_x$ ZN, and 6-WO$_x$ ZN samples. Reaction conditions: 1.5 h^{-1} of weight hour space velocity (WHSV); 100 mg of catalyst.

The detailed product distributions of the WO$_x$-MFI ZN samples were investigated and compared. At a reaction temperature of 450 °C, ethylene selectivity decreased in the following order: 1-WO$_x$ ZN (~92.86%) > 2-WO$_x$ ZN (~92.54%) 6-WO$_x$ ZN (92.44%) > 4-WO$_x$ ZN(91.07%) (Table 4). That is, highly dispersed WO$_x$ nanoparticles supported by 1-WO$_x$ ZN and 2-WO$_x$ ZN exhibited higher selectivity for ethylene, as compared with the larger WO$_x$ nanoparticles on the other samples. In the case of 4- and 6-WO$_x$ ZN, relatively large amounts of acetaldehyde were generated. As mentioned before, it was proposed that acetaldehyde synthesis proceeds via alpha C-H scission in ethanol and hydrogen release. This release might hydrogenate ethylene to form the ethane molecule [40].

Table 4. EtOH conversion and ethylene selectivity [a] of 1-WO$_x$ ZN, 2-WO$_x$ ZN, 4-WO$_x$ ZN, and 6-WO$_x$ ZN samples.

Sample	Ethylene Selectivity	Ethane Selectivity	Acetaldehyde Selectivity	Diethyl Ether Selectivity	Etc Selectivity
1-WOx-ZN	92.86% (0.041 [b])	2.43% (0.002 [b])	2.37% (0.006 [b])	0.36% (0.001 [b])	1.97% (0.033 [b])
2-WOx-ZN	92.54% (0.535 [b])	2.34% (0.082 [b])	2.95% (0.456 [b])	0.29% (0.033 [b])	1.90% (0.134 [b])
4-WOx-ZN	91.07% (0.591 [b])	2.59% (0.143 [b])	4.38% (0.297 [b])	0.29% (0.043 [b])	1.69% (0.736 [b])
6-WOx-ZN	92.44% (0.083 [b])	1.23% (0.837 [b])	4.51% (0.484 [b])	0.27% (0.277 [b])	1.55% (0.712 [b])

[a] Reaction conditions: WHSV was 1.5 h^{-1}; reaction temperature was 45 °C; 100mg of catalyst. [b] Standard deviation.

To investigate the effect of water in ethanol dehydration, pure ethanol in a saturator was replaced by an aqueous solution of ethanol (5 wt % H$_2$O/95 wt % EtOH) and the catalytic performance as a function of temperature was measured. Figure S5 showed that EtOH conversion relatively increased in the temperature range of 360 °C to 450 °C, while ethylene selectivity decreased over the whole tested temperature range.

2.3. Operational Stability Testing

Stability testing was performed on 1- and 4-WO$_x$ ZN for 18 h and 48 h, respectivtay, at a reaction temperature of 420 °C and a WHSV of 1.5 h^{-1} (Figure 7). As the figure shows, 1-WO$_x$ ZN was rapidly deactivated and the ethylene yield reduced from 79% to 55% after 18 h of reaction, whereas 4-WO$_x$ ZN was not deactivated even after 48 h of reaction. Note that 4-WO$_x$-ZN samples had an ethanol yield of 84% after reaction for 30 min, but a yield of 93% after 48 h. This increase in catalytic stability may have been due to the rod-like structure of tungsten oxide on 4-WO$_x$-ZN samples and resistance to coke accumulation during the reaction.
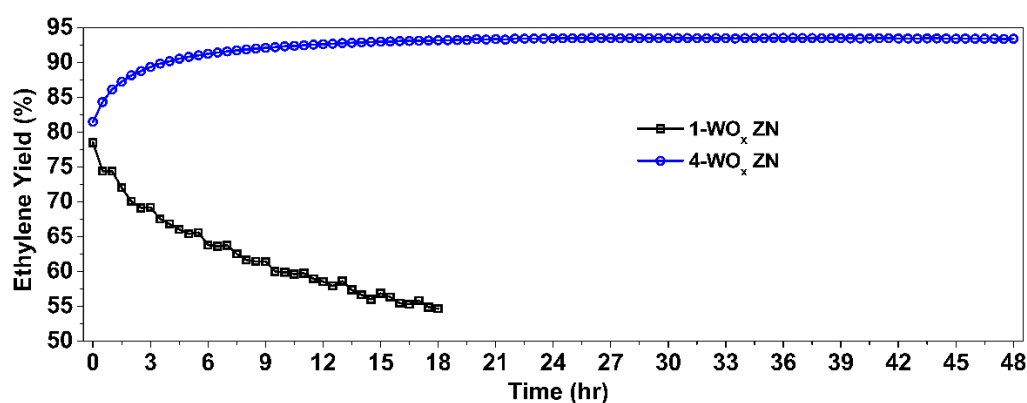
Figure 7. Ethylene yield changes as a function of reaction time for 1-WO$_x$ ZN and 4-WO$_x$ ZN samples over 18 h and 48 h, respectively. Reaction conditions: WHSV was 1.5 h^{-1}; reaction temperature was 420 °C; 100 mg of catalyst.

XRD, N$_2$ isotherms, and elemental analysis (EA) of the 1-WO$_x$ ZN sample after the reactions were used to investigate the cause of deactivation (Figure S6 for XRD pattern). The XRD pattern of 1-WO$_x$ ZN did not change after the reaction, which suggested that metal sintering was not the main reason for deactivation. In addition, BET surface area and pore volume were similar before and after the reaction, showing that deactivation was not due to the collapse of the pore structure. The elemental analyzer (EA) results revealed that the 1-WO$_x$ ZN sample contained 7% of carbon after 18 h of reaction. Based on the EA results, it appeared that the coke may have covered active sites, thus preventing ethanol access and reducing EtOH conversion. The 1-WO$_x$ ZN sample was regenerated under an air flow of 20 mL min^{-1} at 550 °C for coke removal. After regeneration, the 1-WO$_x$ ZN sample was tested again in the dehydration of ethanol reaction under the same conditions. As shown in Figure S7, the ethylene yield at 30 mins decreased from 78.5% to 70.6%. However, the deactivation rate was similar to the fresh 1-WO$_x$ ZN sample. The decrease in initial yield could be attributed to the particle sintering or the collapse of the pore structure during the regeneration process.

3. Materials and Methods

3.1. Materials

1-Bromooctadecane (>97.0%) and N,N,N',N'-tetramethyl-1,6-diaminohexane (>98.0%) were purchased from TCI (Tokyo Chemical Industries). Ammonium metatungstate hydrate (99.99%), 1-bromobutane (99%), and silica (fumed powder) were purchased from Aldrich. Absolute ethanol (≥99.9%) was purchased from Merck and sodium hydroxide was purchased from Daejung.

3.2. Preparation of Tungsten Oxide Impregnated MFI Zeolite Nanosheets

Diammonium surfactant (C$_{18}$H$_{37}$-N$^+$(Me)$_2$-C$_6$H$_{12}$-N$^+$(Me)$_2$-C$_4$H$_9$) was used as an MFI zeolite SDA and was synthesized as previously described [26]. Diammonium surfactant was dissolved in distilled water containing sodium hydroxide and the resulting solution was mixed with fumed silica and stirred at room temperature for 2 h. The molar composition of the final reaction mixture for the MFI zeolite nanosheet production was 100 SiO$_2$:7.5 diammonium surfactant:10 Na$_2$O:6000 H$_2$O. This mixture was heated at 150 °C for 77 h with tumbling in an autoclave. After the hydrothermal reaction, the reaction gel obtained was filtered to obtain precipitates, which were dried in an oven at 100 °C and calcined at 550 °C for 4 h.

Calcined MFI zeolite nanosheets were impregnated with tungsten oxides using the incipient wetness impregnation method [43,44]. In a typical preparation, ammonium metatungstate hydrate was dissolved in 0.53 mL of distilled water and 1 g of MFI nanosheets were dipped into this solution for 2 h. Samples were then dried and calcined at 550 °C for 4 h under flowing air.

3.3. Characterization

X-ray diffraction (XRD) patterns were obtained using a Rigaku Miniflex instrument with a Cu Kα source (λ = 0.154 nm) operated at 30 kV and 15 mA. The step-scan mode was applied with a count time of 3 s and the XRD measurement was for 4 s with an angle interval of 0.01°. N_2 adsorption–desorption was measured using a Micrometrics Tristar II 3020 instrument at 77 K. Before measurements, samples were degassed at 300 °C at least for 2 h. Brunauer–Emmett–Teller surface areas were calculated using the BET equation using adsorption data obtained at P/P_0 ratios between 0.05 and 0.3. NH_3-TPD was performed using a Micrometrics Autochem II 2920 instrument. To obtain the NH_3-TPD spectra, samples were pre-treated under flowing He (50 mLmin^{-1}) at 500 °C for 1 hour. After cooling to 100 °C, samples were saturated with NH_3 for 2 h, then physically adsorbed NH_3 was removed by placing samples in flowing nitrogen for 1 h. TPD NH_3 curves were obtained in the temperature range of 100–600 °C using a ramping rate of 10 °Cmin^{-1}. Elemental analysis was performed using a Thermos EA1112 unit. STEM images were obtained using an FEI Titan ETEM (Environmental transmission electron microscopy) G2 microscope equipped with a Cs corrector and a monochromatic electron beam at an acceleration voltage of 300 kV (Institute for Basic Science). TEM images were obtained using a JEM-ARM200F (JEOL) with an electron beam at an acceleration voltage of 300 kV. Before TEM and STEM measurement, the sample was added to EtOH solvent and sonicated for 30 min for dispersion. Then, the EtOH solution containing the sample was added dropwise to the copper grid for EM measurement. X-ray absorption spectroscopy (XAS) spectra were recorded using beamline 10 C at the Pohang Accelerator Laboratory (PAL, Pohang, South Korea) using monochromatic synchrotron produced X-rays of beam energy 2.5 GeV and a beam current of 360 mA. XAS measurements were carried out at the W-L$_3$ edge (7709 eV) using energy scans from 10,006 to 11,180 eV, which included XANES (X-ray near edge structure) and EXAFS (extended X-ray absorption fine structure) regions. All XAS data were acquired in transmission mode.

3.4. Catalytic Test

Ethanol to ethylene conversion was performed using a fixed-bed reactor made of Pyrex®. Prior to loading the catalyst, it was pelletized, ground, and sieved to provide 0.250 to 0.355 mm diameter particles, which were then loaded (100 mg) into the Pyrex® reactor. The internal diameter of the Pyrex® reactor was 6.7 mm. A thermocouple was located just above the catalyst to record the temperatures. Before the reaction, the catalyst was activated at 550 °C for 2 h under flowing N_2 (50 mLmin^{-1}). After cooling to 300 °C, N_2 (17.3 mLmin^{-1}) was passed through the anhydrous ethanol saturator, which held at a temperature of 18 °C and a WHSV of 1.5 h^{-1}. Reaction temperatures varied from over 300 to 450 °C. Reaction products were analyzed using an online gas chromatograph (Agilent, 7980A) equipped with a flame ionization detector and an Rt-U bond capillary column from Restek.

4. Conclusions

Tungsten oxides, in forms of small (<2 nm) or needle-like nanoparticles, were impregnated into MFI zeolite. Small nanoparticles exhibited high ethylene selectivity at high reaction temperatures (>390 °C), but were rapidly deactivated due to rapid coke formation. On the other hand, needle-like WO$_x$ had a longer catalytic lifetime, but a selectivity slightly lower than that of small WO$_x$ nanoparticles. Importantly, due to their high hydrothermal stabilities, the porosities of MFI zeolite nanosheets were not diminished during EtOH dehydration. We believe that the use of hydrothermal stable zeolite as catalytic support for metal or metal oxide nanoparticles offers a promising means of conducting catalytic reactions, in which water is generated as a byproduct.

Supplementary Materials: The following are available online at http://www.mdpi.com/2073-4344/9/8/670/s1, Figure S1: (**a**) SEM and (**b**) TEM results and (**c**) XRD patterns of MFI zeolite nanosheets; Figure S2: A typical W-L$_3$ XANES spectrum of W^{6+} in monoclinic WO$_3$; Figure S3: Oscillation wavelengths of 1-WO$_x$ ZN, 2-WO$_x$ ZN, 4-WO$_x$ ZN, and 6-WO$_x$ ZN samples; Figure S4: Typical gas chromatograms obtained by online analysis showing ethylene, ethane, acetaldehyde, and diethyl ether peaks; Figure S5. (**a**) Ethanol conversion and (**b**) selectivity

as a function of reaction temperature over 4-WOx ZN sample with ethanol containing 5 wt % water. Reaction conditions: 1.5 h^{-1} of WHSV, 100mg catalyst; Figure S6: The XRD pattern of 1-WO$_x$ ZN after an 8 h catalytic reaction; Table S1: Comparison of the catalytic reaction with commercial catalysts and ZN samples over 8 h; Figure S7: Ethanol yield changes as a function of reaction time for 1-WOx ZN samples after regeneration. Reaction conditions: WHSV—1.5 h^{-1}, reaction temperature—420 °C, and 100 mg of catalyst.

Author Contributions: Conceptualization, C.J.; methodology, C.J., H.K.; formal analysis, H.K.; investigation, H.K., M.N.; writing, C.J., M.N.; visualization, H.K.

Conflicts of Interest: The authors have no conflict of interest to declare.

References

1. Amghizar, I.; Vandewalle, L.A.; van Geem, K.M.; Marin, G.B. New Trends in Olefin Production. *Engineering* **2017**, *3*, 171–178. [CrossRef]
2. Zhang, M.; Yu, Y. Dehydration of Ethanol to Ethylene. *Ind. Eng. Chem. Res.* **2013**, *52*, 9505–9514. [CrossRef]
3. Zacharopoulou, V.; Lemonidou, A. Olefins from Biomass Intermediates: A Review. *Catalysts* **2018**, *8*, 2. [CrossRef]
4. Liu, Y. Catalytic Ethylene Oligomerization over Ni/Al-HMS: A Key Step in Conversion of Bio-Ethanol to Higher Olefins. *Catalysts* **2018**, *8*, 537. [CrossRef]
5. Ren, T.; Patel, M.; Blok, K. Olefins from conventional and heavy feedstocks: Energy use in steam cracking and alternative processes. *Energy* **2006**, *31*, 425–451. [CrossRef]
6. Benchaita, T. *Greenhouse Gas Emissions from New Petrochemical Plants*; Inter-American Development Bank: Washington, DC, USA, 2013.
7. Moon, S.; Chae, H.-J.; Park, M.B. Dehydration of Bioethanol to Ethylene over H-ZSM-5 Catalysts: A Scale-Up Study. *Catalysts* **2019**, *9*, 186. [CrossRef]
8. Fan, D.; Dai, D.-J.; Wu, H.-S. Ethylene Formation by Catalytic Dehydration of Ethanol with Industrial Considerations. *Materials (Basel)* **2012**, *6*, 101–115. [CrossRef]
9. Arenamnart, S.; Trakarnpruk, W. Ethanol Conversion to Ethylene Using Metal-Mordenite Catalysts. *Int. J. App. Sci. Eng.* **2006**, *4*, 21–32.
10. Wu, C.-Y.; Wu, H.-S. Ethylene Formation from Ethanol Dehydration Using ZSM-5 Catalyst. *ACS Omega* **2017**, *2*, 4287–4296. [CrossRef]
11. Madeira, F.F.; Gnep, N.S.; Magnoux, P.; Maury, S.; Cadran, N. Ethanol transformation over HFAU, HBEA and HMFI zeolites presenting similar Brønsted acidity. *Appl. Catal. A: Gen.* **2009**, *367*, 39–46. [CrossRef]
12. Xin, H.; Li, X.; Fang, Y.; Yi, X.; Hu, W.; Chu, Y.; Zhang, F.; Zheng, A.; Zhang, H.; Li, X. Catalytic dehydration of ethanol over post-treated ZSM-5 zeolites. *J. Catal.* **2014**, *312*, 204–215. [CrossRef]
13. Arai, H.; Take, J.-I.; Saito, Y.; Yoneda, Y. Ethanol dehydration on alumina catalysts: I. The thermal desorption of surface compounds. *J. Catal.* **1967**, *9*, 146–153. [CrossRef]
14. Pan, Q.; Ramanathan, A.; Snavely, W.K.; Chaudhari, R.V.; Subramaniam, B. Synthesis and Dehydration Activity of Novel Lewis Acidic Ordered Mesoporous Silicate: Zr-KIT-6. *Ind. Eng. Chem. Res.* **2013**, *52*, 15481–15487. [CrossRef]
15. Zhang, X.; Wang, R.; Yang, X.; Zhang, F. Comparison of four catalysts in the catalytic dehydration of ethanol to ethylene. *Microporous Mesoporous Mater.* **2008**, *116*, 210–215. [CrossRef]
16. Phung, T.K.; Proietti Hernández, L.P.; Lagazzo, A.; Busca, G. Dehydration of ethanol over zeolites, silica alumina and alumina: Lewis acidity, Brønsted acidity and confinement effects. *Appl. Catal. A: Gen.* **2015**, *493*, 77–89. [CrossRef]
17. Takahara, I.; Saito, M.; Inaba, M.; Murata, K. Dehydration of Ethanol into Ethylene over Solid Acid Catalysts. *Catal. Lett.* **2005**, *105*, 249–252. [CrossRef]
18. Zhu, H.; Ramanathan, A.; Wu, J.-F.; Subramaniam, B. Genesis of Strong Brønsted Acid Sites in WZr-KIT-6 Catalysts and Enhancement of Ethanol Dehydration Activity. *ACS Catal.* **2018**, *8*, 4848–4859. [CrossRef]

19. Autthanit, C.; Jongsomjit, B. Production of Ethylene through Ethanol Dehydration on SBA-15 Catalysts Synthesized by Sol-gel and One-step Hydrothermal Methods. *J. Oleo Sci.* **2018**, *67*, 235–243. [CrossRef]

20. Nandiwale, K.Y.; Danby, A.M.; Ramanathan, A.; Chaudhari, R.V.; Subramaniam, B. Zirconium-Incorporated Mesoporous Silicates Show Remarkable Lignin Depolymerization Activity. *ACS Sustainable Chem. Eng.* **2017**, *5*, 7155–7164. [CrossRef]

21. Haishi, T.; Kasai, K.; Iwamoto, M. Fast and Quantitative Dehydration of Lower Alcohols to Corresponding Olefins on Mesoporous Silica Catalyst. *Chem. Lett.* **2011**, *40*, 614–616. [CrossRef]

22. Ramanathan, A.; Maheswari, R.; Barich, D.H.; Subramaniam, B. Niobium incorporated mesoporous silicate, Nb-KIT-6: Synthesis and characterization. *Microporous Mesoporous Mater.* **2014**, *190*, 240–247. [CrossRef]

23. Ramanathan, A.; Subramaniam, B.; Badloe, D.; Hanefeld, U.; Maheswari, R. Direct incorporation of tungsten into ultra-large-pore three-dimensional mesoporous silicate framework: W-KIT-6. *J Porous Mater.* **2012**, *19*, 961–968. [CrossRef]

24. Osman, A.I.; Abu-Dahrieh, J.K.; Rooney, D.W.; Thompson, J.; Halawy, S.A.; Mohamed, M.A. Surface hydrophobicity and acidity effect on alumina catalyst in catalytic methanol dehydration reaction. *J. Chem. Technol. Biotechnol.* **2017**, *92*, 2952–2962. [CrossRef] [PubMed]

25. Choi, M.; Na, K.; Kim, J.; Sakamoto, Y.; Terasaki, O.; Ryoo, R. Stable single-unit-cell nanosheets of zeolite MFI as active and long-lived catalysts. *Nature* **2009**, *461*, 246–249. [CrossRef] [PubMed]

26. Na, K.; Jo, C.; Kim, J.; Cho, K.; Jung, J.; Seo, Y.; Messinger, R.J.; Chmelka, B.F.; Ryoo, R. Directing zeolite structures into hierarchically nanoporous architectures. *Science* **2011**, *333*, 328–332. [CrossRef] [PubMed]

27. Jo, C.; Cho, K.; Kim, J.; Ryoo, R. MFI zeolite nanosponges possessing uniform mesopores generated by bulk crystal seeding in the hierarchical surfactant-directed synthesis. *Chem. Commun.* **2014**, *50*, 4175–4177. [CrossRef]

28. Kim, Y.; Kim, K.; Ryoo, R. Cooperative Structure Direction of Diammonium Surfactants and Sodium Ions to Generate MFI Zeolite Nanocrystals of Controlled Thickness. *Chem. Mater.* **2017**, *29*, 1752–1757. [CrossRef]

29. Na, K.; Choi, M.; Park, W.; Sakamoto, Y.; Terasaki, O.; Ryoo, R. Pillared MFI zeolite nanosheets of a single-unit-cell thickness. *J. Am. Chem. Soc.* **2010**, *132*, 4169–4177. [CrossRef]

30. Park, W.; Yu, D.; Na, K.; Jelfs, K.E.; Slater, B.; Sakamoto, Y.; Ryoo, R. Hierarchically Structure-Directing Effect of Multi-Ammonium Surfactants for the Generation of MFI Zeolite Nanosheets. *Chem. Mater.* **2011**, *23*, 5131–5137. [CrossRef]

31. Cho, J.; Xu, L.; Jo, C.; Ryoo, R. Highly monodisperse supported metal nanoparticles by basic ammonium functionalization of mesopore walls for industrially relevant catalysis. *Chem. Commun.* **2017**, *53*, 3810–3813. [CrossRef]

32. Luo, H.Y.; Bui, L.; Gunther, W.R.; Min, E.; Román-Leshkov, Y. Synthesis and Catalytic Activity of Sn-MFI Nanosheets for the Baeyer–Villiger Oxidation of Cyclic Ketones. *ACS Catal.* **2012**, *2*, 2695–2699. [CrossRef]

33. Wu, Y.; Emdadi, L.; Oh, S.C.; Sakbodin, M.; Liu, D. Spatial distribution and catalytic performance of metal–acid sites in Mo/MFI catalysts with tunable meso-/microporous lamellar zeolite structures. *J. Catal.* **2015**, *323*, 100–111. [CrossRef]

34. Kim, J.; Kim, W.; Seo, Y.; Kim, J.-C.; Ryoo, R. n-Heptane hydroisomerization over Pt/MFI zeolite nanosheets: Effects of zeolite crystal thickness and platinum location. *J. Catal.* **2013**, *301*, 187–197. [CrossRef]

35. Gong, P.; Li, B.; Kong, X.; Liu, J.; Zuo, S. Well-dispersed Ni nanoclusters on the surfaces of MFI nanosheets as highly efficient and selective catalyst for the hydrogenation of naphthalene to tetralin. *Appl. Sur. Sci.* **2017**, *423*, 433–442. [CrossRef]

36. Ponnusamy, R.; Gangan, A.; Chakraborty, B.; Sekhar Rout, C. Tuning the pure monoclinic phase of WO3 and WO3-Ag nanostructures for non-enzymatic glucose sensing application with theoretical insight from electronic structure simulations. *J. Appl. Phys.* **2018**, *123*, 24701. [CrossRef]

37. Kübel, C.; Voigt, A.; Schoenmakers, R.; Otten, M.; Su, D.; Lee, T.-C.; Carlsson, A.; Bradley, J. Recent advances in electron tomography: TEM and HAADF-STEM tomography for materials science and semiconductor applications. *Microsc. Microanal.* **2005**, *11*, 378–400. [CrossRef] [PubMed]

38. Yamazoe, S.; Hitomi, Y.; Shishido, T.; Tanaka, T. XAFS Study of Tungsten L1- and L3-Edges: Structural Analysis of WO_3 Species Loaded on TiO_2 as a Catalyst for Photo-oxidation of NH_3. *J. Phys. Chem. C* **2008**, *112*, 6869–6879. [CrossRef]

39. Chladek, P.; Coleman, L.J.I.; Croiset, E.; Hudgins, R.R. Gas chromatography method for the characterization of ethanol steam reforming products. *J. Chromatogr. Sci.* **2007**, *45*, 153–157. [CrossRef]

40.　DeWilde, J.F.; Czopinski, C.J.; Bhan, A. Ethanol Dehydration and Dehydrogenation on γ-Al$_2$O$_3$: Mechanism of Acetaldehyde Formation. *ACS Catal.* **2014**, *4*, 4425–4433. [CrossRef]

41.　Kang, M.; Bhan, A. Kinetics and mechanisms of alcohol dehydration pathways on alumina materials. *Catal. Sci. Technol.* **2016**, *6*, 6667–6678. [CrossRef]

42.　DeWilde, J.F.; Chiang, H.; Hickman, D.A.; Ho, C.R.; Bhan, A. Kinetics and Mechanism of Ethanol Dehydration on γ-Al$_2$O$_3$: The Critical Role of Dimer Inhibition. *ACS Catal.* **2013**, *3*, 798–807. [CrossRef]

43.　El-Bahy, Z.M.; Mohamed, M.M.; Zidan, F.I.; Thabet, M.S. Photo-degradation of acid green dye over Co-ZSM-5 catalysts prepared by incipient wetness impregnation technique. *J. Hazard. Mater.* **2008**, *153*, 364–371. [CrossRef] [PubMed]

44.　Yan, Y.; Jiang, S.; Zhang, H. Catalytic wet oxidation of phenol with Fe–ZSM-5 catalysts. *RSC Adv.* **2016**, *6*, 3850–3859. [CrossRef]